Journal of Alloys and Compounds 615 (2014) 546–552

Contents lists available at ScienceDirect

Journal of Alloys and Compounds

journal homepage: www.elsevier.com/locate/jalcom

# Thermoelectric properties of nanostructured bismuth–telluride thin films grown using pulsed laser deposition

Phuoc Huu Le [a], Chien-Neng Liao [b], Chih Wei Luo [c,1], Jihperng Leu [a,*]

[a] Department of Materials Science and Engineering, National Chiao Tung University, Hsinchu 30049, Taiwan, ROC
[b] Department of Materials Science and Engineering, National Tsing-Hua University, Hsinchu 30013, Taiwan, ROC
[c] Department of Electrophysics, National Chiao Tung University, Hsinchu 30010, Taiwan, ROC

ARTICLE INFO

*Article history:*
Received 4 February 2014
Received in revised form 21 May 2014
Accepted 2 July 2014
Available online 10 July 2014

*Keywords:*
$Bi_2Te_3$
Thermoelectric properties
Nanostructures
Pulsed laser deposition (PLD)

ABSTRACT

Nanostructured n-type bismuth telluride ($Bi_2Te_3$) thin films were grown on $SiO_2$/Si (100) substrates at argon ambient pressure ($P_{Ar}$) of 80 Pa by pulsed laser deposition (PLD). The effects of film morphologies, structures, and compositions on the thermoelectric properties were investigated. At a substrate temperature ($T_s$) of 220–340 °C, stoichiometric films with highly (00l)-oriented and layered structures showed the best properties, with a carrier mobility $\mu$ of 83.9–122.3 $cm^2$/Vs, an absolute Seebeck coefficient $|\alpha|$ of 172.8–189.7 μV/K, and a remarkably high power factor (PF) of 18.2–24.3 μW $cm^{-1}$ $K^{-2}$. By contrast, the Te-rich films deposited at $T_s \leqslant 120$ °C with (015)-preferred orientations and columnar-small grain structures or the Te-deficient film deposited at 380 °C with $Bi_4Te_5$ polyhedron structure possessed poor properties, with $\mu < 10.0$ $cm^2$/Vs, $|\alpha| < 54$ μV/K, and PFs $\leqslant 0.44$ μW $cm^{-1}$ $K^{-2}$. The morphology of highly (00l) oriented-layered structures and the stoichiometry predominantly contribute to the substantial enhancement of $\mu$ and $|\alpha|$, respectively, resulting in remarkable enhancement in PF.



## 1. Introduction

Thermoelectric (TE) materials are of interests for applications as heat pumps and power generators [1–4]. The performance of TE materials is evaluated in terms of a dimensionless figure of merit, $ZT = \alpha^2\sigma T/\kappa$, in which $\alpha$, $\sigma$, $\kappa$, and $T$ are the Seebeck coefficient, the electrical conductivity, the thermal conductivity, and absolute temperature, respectively. To achieve a high ZT value, a TE material must exhibit a high power factor (PF), $\alpha^2\sigma$, and low thermal conductivity, $\kappa$. However, increasing the ZT value is challenging because of the coupling among the TE parameters [3]: the relationship between $\alpha$ and the carrier concentration $n$ (expressed by $|\alpha| \sim n^{-2/3}$ [3]) limits the enhancement of the PF ($=\alpha^2\sigma$), whereas the proportional relationship between electrical conductivity and electronic thermal conductivity (the Wiedmann–Franz law) restricts the improvement of the $\sigma/\kappa$ ratio.

Bismuth telluride ($Bi_2Te_3$)-based materials have been widely exploited for Peltier-coolers and thermoelectric generators at low temperature regime [5–8]. Nanocrystalline and nanostructured $Bi_2Te_3$-based films conduct heat poorly because of extensive phonon scattering at grain boundaries [9–12], but the electrical transport properties of the films are impaired because of lattice imperfections and grain-boundary defects [9], indicating that further investigation is required to determine how to improve PF or the electronic part of ZT. Currently, enhancing the PF of $Bi_2Te_3$-based thin films is challenging. Besides the coupling among TE material properties [3], the control of film stoichiometry is a key factor for obtaining better TE properties [13–16]. Yet, it is a challenge to grow stoichiometric films because of the tendency for re-evaporation of volatile elements (i.e. Te, Se) at elevated $T_s$ [15,16], and the low sticking coefficient Te (<0.6) at $T_s$ beyond 300 °C [17,18]. Numerous charge carriers arising from vacancy defects of volatile elements can constrain the enhancement of $|\alpha|$; however, low carrier concentrations can suppress electrical conductivity if carrier mobility ($\mu$) is poor.

Substantial effort has been devoted to enhancing the PF and ZT values of $Bi_2Te_3$ thin films grown using various vapor-deposition techniques. Moreover, nanocrystalline and nanostructured $Bi_2Te_3$ thin films have recently attracted considerable attention because they exhibit superior TE performance [9,10,13,19–22]. The layered-hexagonal $Bi_2Te_3$ films fabricated using radio-frequency magnetron sputtering possessed a PF of 8.8 μW $cm^{-1}$ $K^{-2}$ for an (015)-oriented film, and a PF of 33.7 μW $cm^{-1}$ $K^{-2}$ for a highly (00l)-oriented layered film [19,21]. Furthermore, PFs of 27 μW $cm^{-1}$ $K^{-2}$ and 39.9 μW $cm^{-1}$ $K^{-2}$ were measured for

* Corresponding author. Tel.: +886 35131420.
*E-mail addresses:* cwluo@mail.nctu.edu.tw (C.W. Luo), jimleu@mail.nctu.edu.tw (J. Leu).
[1] Tel.: +886 35712121x56196.

http://dx.doi.org/10.1016/j.jallcom.2014.07.018
0925-8388/

smooth-epitaxial- and hexagonal-$Bi_2Te_3$ films grown using molecular beam epitaxy (MBE) [23] and co-evaporation [24], respectively. In the case of pulsed laser deposition (PLD), tightly controlling substrate temperatures ($T_s$) and ambient pressures enables the morphologies and compositions of films to be manipulated extensively, which offers a new method for enhancing the TE properties of films [13,16,20,25,26]. For example, self-assembled $Bi_2Te_3$ films featuring well-aligned zero- to three-dimensional nanoblocks have been fabricated, but the room-temperature PFs of these films remain low ($\leqslant$1.9 $\mu W\,cm^{-1}\,K^{-2}$) [20]. By contrast, Li Bassi et al. [13] obtained high room-temperature PFs of approximately 21.2 and 50.6 $\mu W\,cm^{-1}\,K^{-2}$ for compact-smooth and layered-smooth $Bi_2Te_3$ films, respectively. Therefore, the interrelationships between PLD processing conditions, microstructures, and TE properties of $Bi_2Te_3$-based thin films must be understood comprehensively.

In this study, the advantageous features of the PLD technique were exploited and a wide range of $T_s$ of 30–380 °C was used to grow various $Bi_2Te_3$ thin films featuring well-defined morphologies and grain sizes ranging from the nanoscale to the microscale. The PFs of the films were substantially enhanced because the resulting improvement in crystal structure enabled attaining high $\mu$ values and concurrently achieving stoichiometry, which lowered $n$ and enhanced $|\alpha|$ (obeying $|\alpha| \sim n^{-2/3}$ approximately). A comprehensive understanding of TE $Bi_2Te_3$-based thin films grown using PLD is presented in this study.

## 2. Experimental details

Bismuth telluride thin films were deposited on $SiO_2$ (300 nm)/Si (100) substrates (size of 15 × 15 $mm^2$) at $T_s$ of 30–380 °C and $P_{Ar}$ of 80 Pa using PLD. The substrate was heated and maintained at desired $T_s$ using a thermocouple and a PID temperature controller. The thermocouple was buried inside a stainless-steel substrate holder which was heated by a tungsten lamp just behind the holder. The UV pulses (20 ns duration) from a KrF excimer laser ($\lambda$ = 248 nm, repetition: 5 Hz) were focused on a stoichiometric polycrystalline $Bi_2Te_3$ target (purity 99.99%) with fluence of 3.8 $J/cm^2$; the target-to-substrate distance was 40 mm. The number of laser pulses was 12,000 and deposition took 40 min. The average growth rate was approximately 0.52 Å/pulse. An approximately 300-nm-thick $SiO_2$ layer was thermally grown on the Si substrates for electrical isolation purpose.

The orientation and crystallinity of $Bi_2Te_3$ films were determined using X-ray diffraction (XRD, Bruker D8) with Cu Kα radiation ($\lambda$ = 1.5406 Å) in $2\theta - \omega$ and rocking-curve ($\omega$-scan) configurations. Digital HRTEM images were obtained using high-resolution transmission electron microscopy (HRTEM, Philips Tecnai F20) operated at 200 kV, and Gatan 2 k × 2 k charged couple device camera. The specimens were prepared using a standard procedure of mechanical thinning and Ar-ion milling. Surface morphology and film thickness were examined using field-emission scanning electron microscopy (SEM, JEOL JSM-6500) through plane-view and cross-sectional images, respectively. Film compositions were also analyzed using an Oxford energy-dispersive X-ray spectroscopy (EDS) equipped with the SEM instrument at an accelerating voltage of 15 kV, a dead time of 22–30%, and a collecting time of 60 s. The atomic percentage of each film was determined by averaging the values measured in 5 or more distinct 13 × 18 $\mu m^2$ areas on the surface of films. The in-plane electrical conductivity, carrier concentration, and mobility were measured at room temperature using a Hall system (Bio-Rad HL5500PC) with van der Pauw geometry. Indium balls were used to improve ohmic contact on the films' surface. The in-plane Seebeck coefficient at room temperature was determined from the slope of the voltage difference vs. the temperature difference curve, based on a static temperature-difference method [27].

## 3. Results and discussion

Fig. 1 presents the cross-section and top-view SEM images of $Bi_2Te_3$ thin films grown at $T_s$ ranging from 30 to 380 °C at $P_{Ar}$ = 80 - Pa. Under these conditions, films of six well-defined morphologies featuring distinct grain sizes, shapes, and stacking characteristics were successfully prepared. Fig. 2 presents the grain-size distribution and the most probable size (MS) of these films, which were determined using SEM statistical analysis. First, at room temperature (30 °C), 0D columnar nanoparticles (CNPs) were grown, which exhibited the smallest MS (57 nm) and a columnar structure that was approximately 50 nm wide and 400 nm high. Second, at 120 °C, columnar nanoflowers (CNFs) were formed as a result of the stacking of 2D platelets (MS = 73 nm), which generated flower-like structures featuring columns that were approximately 75 nm wide and 500 nm high. Third, at 220 °C, nanodiscs (NDs) were formed that comprised numerous disc-like crystals, whose MS was 287 nm in diameter and 24.5 nm in thickness; the disc thickness was determined by performing 2D fast Fourier transform (FFT, the inset in Fig. 1c) of the dashed-square area indicating a set of discs (Fig. 1c). Fourth, at 300 °C, a layered compact polycrystalline (LCP) film was prepared that exhibited an MS of 477 nm. Intriguingly, this film was formed by compactly stacking of the 3D layered nanoblocks, but it exhibited a relatively rough surface. Fifth, at 340 °C, a layered-triangular-platelet (LTP) structure was prepared that exhibited the largest MS (846 nm, with a layer thickness of 53 nm) and the broadest grain-size distribution (reaching the micron size) (Figs. 1e and 2). Finally, the films deposited at 380 °C displayed a polyhedral (PH) structure that was composed of 3D triangular and polygonal crystals (MS of 785 nm) and exhibited a diminished density because of the presence of microvoids between crystals. The MS and the width of the distribution curves increased monotonically with increasing $T_s$ from RT to 340 °C and then decreased slightly at 380 °C, as shown in Fig. 2 and the inset of Fig. 2.

The $T_s$ used can affect the nucleation and growth of films. At low a $T_s$, the rate of supersaturation is high, which reduces not only the critical size of the nuclei but also the magnitude of the nucleation energy barrier, and thus numerous, small nanoparticles grew at 30 °C and nanoflowers grew at 120 °C [16]. Moreover, the growth mechanism of the columnar structures (Figs. 1a and b) can be attributed to the combined effects of a high deposition rate and a low crystal growth rate: the high $P_{Ar}$ of 80 Pa tightly confines the ablated plume along the direction of the substrate to increase the deposition rate [25], whereas the potentially adsorbed argon limits the mobility of adatoms to suppress the lateral growth of the crystals at low $T_s$ ($\leqslant$120 °C) [28,29]. By contrast, the deposition is faster on the top of islands than in the valleys between the islands with an oblique incident flux (the so-called shadowing effect) [28,30], which generates the separated or voided inter-grain boundaries of columnar structures. The columnar structures present in the $Bi_2Te_3$ films grown here were similar to those in $Bi_2Se_3$ films grown at comparatively high temperatures and pressures (200–250 °C, 173 Pa helium) [16].

At a high $T_s$ ($\geqslant$220 °C), however, a reduction in the supersaturation rate increases the critical size of the nuclei and the nucleation barrier. Consequently, the large nuclei can further create isolated islands and 3D crystal structures on the substrates to minimize the surface energy and interface energy [31,32] by means of surface diffusion, grain-boundary migration, and possible recrystallization. Conversely, the LTP structure might be formed because of the anisotropic bonding configuration of $Bi_2Te_3$ and the inevitable deviations from a uniform growth environment [33–35]. Moreover, both the diffusion of atoms at high $T_s$ ($\geqslant$220 °C) and the naturally layered crystal structure of $Bi_2Te_3$ result in the formation of layered ND, LCP, and LTP structures [33].

Fig. 3a shows the normalized XRD patterns of the $Bi_2Te_3$ target and films. The polycrystalline rhombohedral $Bi_2Te_3$ phase (space group $D_{3d}^5$–$R\bar{3}m$) with (015)-dominant orientation of the target can be confirmed (JCPDS 82-0358). The films grown at $T_s \leqslant$ 340 °C exhibited the $Bi_2Te_3$ phase but no other detectable phases. However, when $T_s$ was increased to 380 °C, the PH film possessed $Bi_4Te_5$ phase (JCPDS 22-0115), which was associated with a composition of approximately 51.5 at.% Te (Fig. 4). Moreover, like the target, the dominant orientation of the CNP (30 °C) and CNF (120 °C) structures was (015). Typically, $Bi_2Te_3$ (015) is the preferred orientation of 1D structures [19,20,36] because this orientation

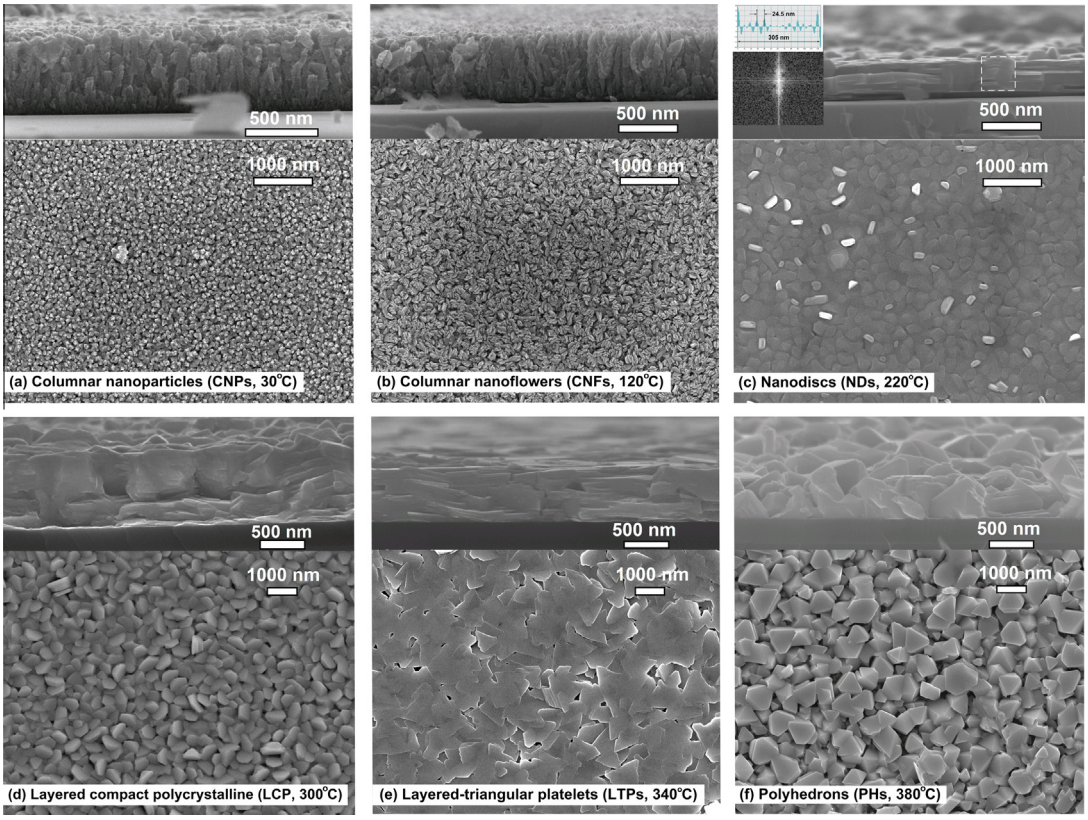


**Fig. 1.** Cross-section and top view SEM images of n-type $Bi_2Te_3$ thin-films with different nanostructures deposited at various substrate temperatures ($T_s$) from 30 to 380 °C under an argon background pressure ($P_{Ar}$) of 80 Pa. The inset in panel (c) shows the FFT patterns and distance profile of the dash square area in the SEM cross-section image.

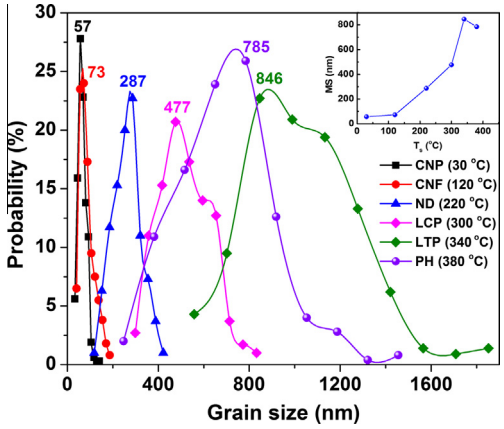


**Fig. 2.** Grain size distributions and the most probable size (MS) of the films in Fig. 1(a–f), which was statistically analyzed from at least 200 grains of top-view SEM images. The inset shows the $T_s$-dependent MS of the films.

supports not only stoichiometric growth but also regular structures that feature a bonding sequence of $\cdots Te^{(1)}$–Bi–$Te^{(2)}$–Bi–$Te^{(1)}\cdots$ [37]. Because the adatom mobility increased at $T_s$ = 220–340 °C, the films featuring ND, LCP, and LTP structures exhibited the highly preferred crystal orientation of {00l}, which possesses the lowest surface energy as a result of the weak $Te^{(1)}\cdots Te^{(1)}$ bond [37].

The crystallinity and grain orientation of the films were determined by measuring X-ray rocking curves. As shown in Fig. 3a, the full width at half maximum (FWHM) of the (006) peak in the $Bi_2Te_3$ phase and the (0011) peak in the $Bi_4Te_5$ phase dropped substantially, from 5.87° in the case of CNFs (at 120 °C) to 0.74° in NDs (at 220 °C), indicating that NDs feature superior crystallinity and grain orientation compared with CNFs. Because of the presence of disoriented grains and a rough surface, the FWHMs of the LCP (at 300 °C) and PH (at 380 °C) structures increased slightly, to 1.82° and 1.49° respectively. By contrast, the LTP film exhibited a small FWHM, 1.05°, which can be attributed to the large (micrometer-scale) grain size, flat surface, and layered structure of the film, reducing the disorientation of crystallites.

HRTEM images performed on the low $\mu$ CNP film and the highest $\mu$ ND film are shown in Fig. 3b and c, respectively. Clearly, Fig. 3b presents some nanoparticles (nanocrystals) with sizes >10 nm. Moreover, the lattice spacing of nanoparticles is approximately 0.323 nm, which corresponds to the value of (015) interplanar distance of the $Bi_2Te_3$ crystal. The white lines in Fig. 3b indicate the orientations of (015) planes. Intriguingly, although the overall (015)-orientation is randomly, it possesses some local preferred orientations as shown by the parallel white lines amongst some close nanocrystals. For the ND (220 °C) film, the lower inset in Fig. 3c shows the film with uniform thickness of approximately 295 nm, and the $SiO_2$ layer with thickness of 300 nm. Furthermore, an HRTEM image (Fig. 3c) obtained from the solid square area in the inset exhibits the projected periods of 0.508 nm along the *c*-axis correspond to the lattice spacing of the (006) planes. Thus, the *c*-axis lattice constant of the film is 30.48 Å of $Bi_2Te_3$, which agrees closely with the value (30.44 Å) presented in JCPDS 82-0358. The other examined areas also present similar results. Consequently, this TEM results further demonstrated the highly (00l)-orientated and crystallized structures of the ND, LCP, LTP films that should facilitate the transport of charge carriers.

The $P_{Ar}$ of 80 Pa was determined to be a suitable background pressure because it allows stoichiometric films to be grown even

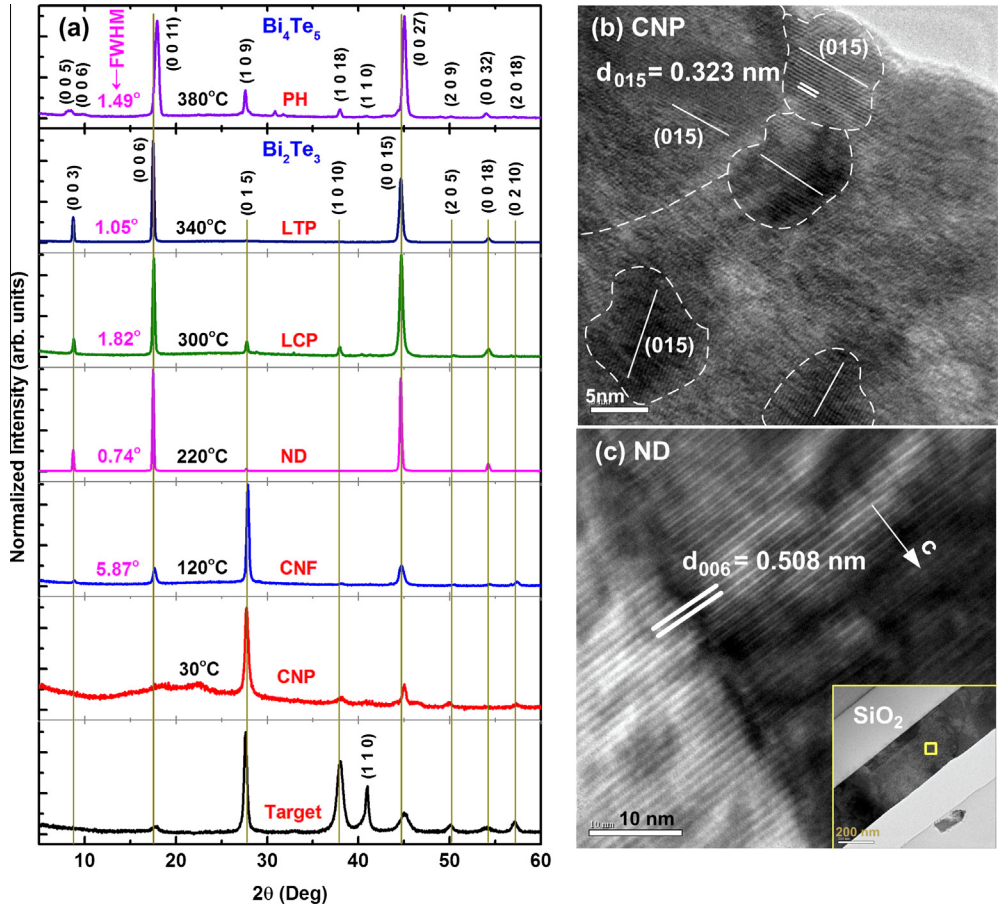


**Fig. 3.** (a) The normalized X-ray diffraction patterns of $Bi_2Te_3$ and $Bi_4Te_5$ thin films. FWHMs of X-ray rocking curves for (006) peak in $Bi_2Te_3$ phase and (0011) peak in $Bi_4Te_5$ phase. (b) An HRTEM image of the columnar nanoparticle (30 °C) film; the white lines indicate the (015) orientation of the nanograins. (c) An HRTEM and a low magnification TEM (inset) images of the nanodisc (220 °C) film.

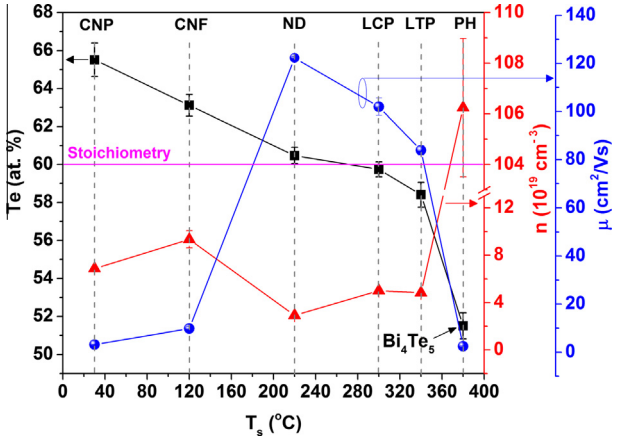


**Fig. 4.** $T_s$-dependent Te at.% (black squares), carrier concentration ($n$, red triangulars), and carrier mobility ($\mu$, blue spheres) of the $Bi_2Te_3$ and $Bi_4Te_5$ films. The abbreviations: CNP, columnar nanoparticle; CNF, columnar nanoflower; ND, nanodisc; LCP, layered compact polycrystalline; LTP, layered triangular platelet; PH, polyhedron. (For interpretation of the references to color in this figure legend, the reader is referred to the web version of this article.)

when the $T_s$ is high (up to 340 °C). We note that low pressures typically increased Te deficiency and elevated $n$, whereas high pressures commonly generated macroscopic droplets on film surfaces. These effects of pressure agree with previous studies on $Bi_2Se_3$ films [16] and with the results described elsewhere [38].

In Fig. 4, the black squares indicate the $T_s$-dependent Te at.% of the six films featuring distinct nanostructures that were deposited at 80-Pa argon. The films clearly exhibited Te enrichment, stoichiometry, and substantial Te deficiency at $T_s \leqslant 120$ °C, 220 °C $\leqslant T_s \leqslant 340$ °C, and $T_s = 380$ °C, respectively. Because the vapor pressure of Te is higher than that of Bi ($P_v^{Te}/P_v^{Bi} \approx 10^5$ at 300 °C [39]), Te reevaporates from heated substrates much faster than Bi does [15,39]. This also occurred in the case of $Bi_2Se_3$ films [40], in which the film composition varied from being Se-rich to stoichiometric to Se-deficient with increasing $T_s$. The Te at.% dropped sharply to approximately 51.5% at 380 °C (Fig. 4), which might be explained by a substantial increase in the Te reevaporation rate and a lowering of the Te sticking coefficient [18].

The variation in the n-type carrier concentration ($n$) and mobility ($\mu$) as a function of $T_s$ and the nanostructures is shown in Fig. 4. The $n$ values of Te-rich films were $6.9 \times 10^{19}$ cm$^{-3}$ (CNPs, at 30 °C) and $9.3 \times 10^{19}$ cm$^{-3}$ (CNFs, at 120 °C), but decreased considerably to range from $2.9 \times 10^{19}$ to $4.9 \times 10^{19}$ cm$^{-3}$ in the case of stoichiometric ND, LCP, and LTP films deposited at 220, 300, and 340 °C, respectively. However, in the highly Te-deficient PH-$Bi_4Te_5$ films deposited at 380 °C, $n$ increased dramatically, reaching approximately $1.06 \times 10^{21}$ cm$^{-3}$. This agreed well with the result in Ref. [13] that the $n$ increased dramatically from $4.9 \times 10^{19}$ cm$^{-3}$ to $5.0 \times 10^{20}$ cm$^{-3}$ with increasing Bi content from 40 at.% (stoichiometry) to 45 at.% ($Bi_4Te_5$ phase). Therefore, the stoichiometry plays a vital role in reducing the $n$ of the films.

The $\mu$ value was inversely proportional to the FWHM and the carrier concentration $n$ (Figs. 3a and 4). The CNP and CNF films

grown at a low $T_s$ (⩽120 °C) had a low $\mu$, <10 $cm^2$/Vs, because of the strong grain-boundary scattering resulting from the columnar structures with small grains (MS of 57 or 73 nm) and the defective scattering centers (ionized impurities). However, in the ND, LCP, and LTP films grown at 220–340 °C, $\mu$ increased substantially and ranged from 83.9 to 122.3 $cm^2$/Vs because of the suppression of those scattering mechanisms, as suggested by the low FWHMs and $n$ results. In addition, the highly (00l)-oriented layered structures with in-plane large crystallites provides a preferential way for electron transport along the *ab*-plane and thus promotes the carrier mobility. Recently, Deng et al. [21] observed that the $\mu$ of the highly (00l)-oriented layered $Bi_2Te_3$ film was approximately 5 times higher than that of the ordinary (015)-oriented film. Despite featuring a large grain size (MS = 785 nm), the $\mu$ in the $Bi_4Te_5$ films displaying the PH structure was small (2.5 $cm^2$/Vs) because of an extremely high carrier concentration ($n = 1.06 \times 10^{21}$ $cm^{-3}$), the difference in phase, and the ordinary 3D-voided structure.

Li Bassi et al. [13] reported that the $\mu$ of Bi-Te films obtained a high value of approximately 100 $cm^2$/Vs only for the stoichiometric $Bi_2Te_3$ film, meanwhile it remained low values of 10–30 $cm^2$/Vs for the other non-stoichiometric Bi–Te films and phases. This result suggests that the stoichiometry plays a certain contribution to the substantially enhanced $\mu$ of the films grown at 220–340 °C. Since the high-$\mu$ preferred structures and the stoichiometry are obtained concurrently in these films, it is hard to fully extract the individual contribution of each factor for the enhanced $\mu$. Nevertheless, under a similar deviation within 2.0 at.% from stoichiometry, the $\mu$ of the 220–340 °C films exhibit a small difference (below 31.5%, Fig. 4) compared to 81.2% for the compact films in Ref. [13]. This weakly $\mu$-dependence on the stoichiometry suggests that microstructure is the predominant factor contributed to the substantial $\mu$ enhancements of the present films.

To explain the evolution of $n$, the antisite and vacancy defects must be considered. From the XRD (006) and (0015) peaks, the averaged $c$-lattice constants of the films were determined using the hexagonal unit cell relation:

$$\frac{1}{d_{hkl}^2} = \frac{4}{3}\left(\frac{h^2+hk+k^2}{a^2}\right) + \frac{\ell^2}{c^2}$$

As shown in the inset in Fig. 5a, the $c$-lattice constant of the CNP and CNF films that were Te-rich is considerably smaller than the standard value of 30.44 Å (JPCDS 82-0358), suggesting the presence of a high density of antisite $Te_{Bi}$ (Te occupying a Bi site, a donor-point defect) because of the smaller atomic radius of Te (1.4 Å) compared with Bi (1.6 Å) [41]. This is to be expected because the strain effect can be neglected for such thick films (thicknesses >530 nm, Fig. 1a and b), and also because $Te_{Bi}$ exhibits the smallest formation energy (approximately 0.5 eV) among point defects such as $Bi_{Te}$ (Bi occupying a Te site) and $V_{Te}$ (Te vacancy) under a Te-rich condition [42,43]. This result suggests that $Te_{Bi}$ is the dominant donor defect that generates the moderate $n$ values of the Te-rich films.

The decrease of $n$ in the stoichiometric ND, LCP, and LTP films was associated with a reduction in the donor defects $Te_{Bi}$ and $V_{Te}$, because the $c$-lattice constant was close to the database value (inset in Fig. 5a). Moreover, the $T_s$ of 220–340 °C should be sufficient for atoms to move and drop to the lowest potential-energy sites and thus reduce the numbers of defects. The structure of the $Bi_4Te_5$ phase can be derived by stacking hexagonal $Bi_2$ and $Bi_2Te_3$ blocks, $(Bi_2)_m(Bi_2Te_3)_n$, and ($m$:$n$ = 1:5), where the –(Bi–Bi)– blocks intercalate in van der Waals gaps between the –($Te^{(1)}$–Bi–$Te^{(2)}$–Bi–$Te^{(1)}$)– blocks [44]. Furthermore, the PH-$Bi_4Te_5$ film remained substantially Te-deficient (approximately 4.1 at.%) when compared with the Te at.% of the EDS results (51.5) and the ideal value of the $Bi_4Te_5$ phase (55.6). Therefore, the dramatic increase of $n$ in the PH-$Bi_4Te_5$ film can be attributed to the dominance of $V_{Te}$ under such Te-deficient (or Bi-rich) conditions, which can also leave Bi interstitials in the lattice and thus generate a $c$-lattice constant that is slightly larger than the database value (JCPDS 22-0115).

Fig. 5a shows the $n$-dependent $|\alpha|$ of the films deposited at various $T_s$. The stoichiometric ND, LCP, and LTP films featuring a low $n$ (2.9–4.9 $\times 10^{19}$ $cm^{-3}$) possessed superior $|\alpha|$ values, ranging from 172.8 to 189.7 μV/K. By contrast, both Te-rich (CNPs and CNFs) and Te-deficient (PHs) films featuring a high $n$ possessed substantially lower $|\alpha|$ values, which ranged from 32.6 to 53.6 μV/K (Fig. 5a). This can be described effectively by the relationship $|\alpha| \sim m^* n^{-2/3}$ in degenerate semiconductors (i.e., the parabolic band, energy-independent scattering approximation [3,16]), as shown in Fig. 5a, in which the solid lines are the plots of the formula in Fig. 5a [3], featuring various effective mass $m^*$ values, ranging from $0.4m_0$ to $1.0m_0$ (where $m_0$ is the free electron mass). Very recently, Shin et al. [45] used $m^* = 0.58m_0$ whose value was inferred from Ref. [4] to describe well their transport results of the $Bi_2Te_3$ nanowires with the similar $n$ of $4.9 \times 10^{19}$–$1.8 \times 10^{20}$ $cm^{-3}$. The present $m^*$ values in the range of $0.4m_0$ –$1.0m_0$ was comparable or slightly larger than the expected value ($0.58m_0$) because various scattering sources, such as the

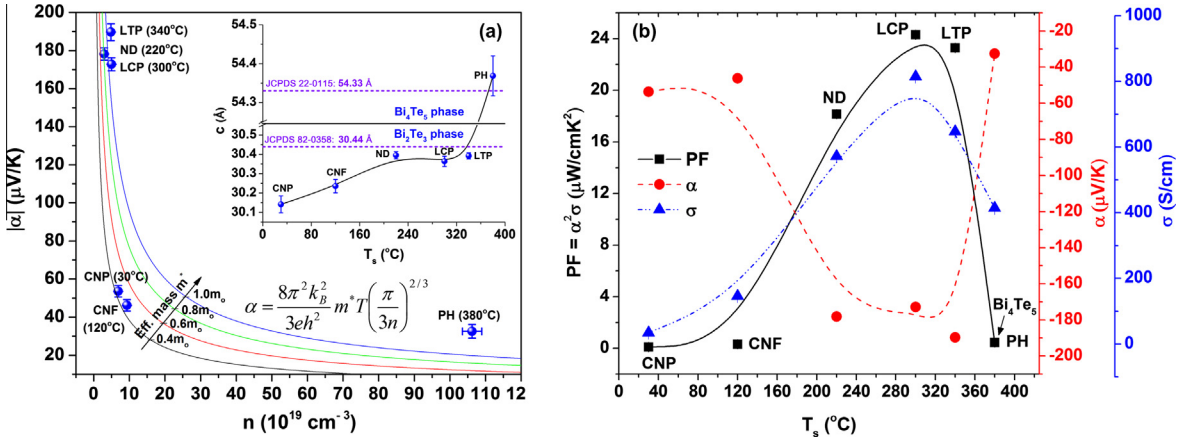


**Fig. 5.** (a) Absolute Seebeck coefficients ($|\alpha|$) vs. $n$; the solid lines are the plots of the formula in Fig. 5a with various effective mass $m^*$ from $0.4m_0$ to $1.0m_0$ ($m_0$ is the free electron mass). Inset: $T_s$-dependent $c$-axis lattice constant of the $Bi_2Te_3$ and $Bi_4Te_5$ films. (b) $T_s$ dependence of room temperature Seebeck coefficient $\alpha$ (red circles), electrical conductivity $\sigma$ (blue triangulars), and power factor (PF = $\alpha^2\sigma$, black squares) of the $Bi_2Te_3$ and $Bi_4Te_5$ films. (For interpretation of the references to color in this figure legend, the reader is referred to the web version of this article.)

**Table 1**
Morphology, growth conditions, method, carrier concentration $n$, carrier mobility $\mu$, electrical conductivity $\sigma$, Seebeck coefficient $\alpha$, power factor PF ($=\alpha^2\sigma$), and Te content of the optimal $Bi_2Te_3$ thin films in this study as compared to properties of $Bi_2Te_3$ thin films reported in the literature. All the selected values were recorded at room temperature.

| Morphology | $T_s$ (°C) | $P_{Ar}$ (Pa) | Method | $n$ ($10^{19}$ cm$^{-3}$) | $\mu$ (cm$^2$/Vs) | $\sigma$ (S/cm) | $\alpha$ (μV/K) | PF (μW/cm K$^2$) | Te (at.%) | Ref. |
|---|---|---|---|---|---|---|---|---|---|---|
| Nanodiscs | 220 | 80 | PLD | 2.9 ± 0.1 | 122.3 ± 0.5 | 572.0 ± 0.06 | −178.2 ± 1.2 | 18.2 ± 0.25 | 60.5 ± 0.4 | This work |
| Layered compact polycrystalline | 300 | 80 | PLD | 5.0 ± 0.2 | 102 ± 3.6 | 814.3 ± 1.5 | −172.8 ± 1.4 | 24.3 ± 0.44 | 59.7 ± 0.4 | This work |
| Layered-triangular platelets | 340 | 80 | PLD | 4.8 ± 0.1 | 83.9 ± 2.0 | 647.3 ± 0.4 | −189.7 ± 2.3 | 23.3 ± 0.57 | 58.4 ± 0.6 | This work |
| Layered-smooth film | 250 | 10 | PLD | 10.1 | 90.6 | 1464.0 | −186 | 50.6 | – | Bassi et al. [13] |
| Compact-smooth film | 350 | 10 | PLD | 3.5 | 95 | 532.0 | −170 | 21.2 | 60 | Bassi et al. [13] |
| Nanoparticles | 300 | 20 | PLD | 9.7 | 14.8 | 230 | −91 | 1.90 | 60 | Chang et al. [20] |
| Layered Structure | 350 | 1.0 | Sputtering | 95 | 12.1 | 1840 | −70 | 8.8 | 56.6 | Deng et al. [19] |
| Highly (00 l)-oriented layered film | 350 | 2.0 | Sputtering | ~10.0 | 52 | ~840.0 | −200 | ~33.7 | ~60 | Deng et al. [21] |
| Hexagonal polycrystalline | 260 | – | Co-evaporation | 1.8 | 125 | 353.4 | −228 | 18.4 | 60 | Silva et al. [46] |
| Hexagonal polycrystalline | 260 | – | Co-evaporation | 6.5 | 75 | 769.2 | −228 | 39.9 | – | Zou et al. [24] |
| Smooth epitaxial surface | 280 | – | MBE | 3.3 | 120 | 670 | −201 | 27 | 60 | Peranio et al. [23] |

grain boundary, lattice, and ionized impurity scatterings, are excluded in the approximation.

Fig. 5b shows the $T_s$-dependent $\alpha$, $\sigma$, and PF ($=\alpha^2\sigma$) of the films. The $\sigma$ value gradually increased from 34.5 ± 0.1 to 814.3 ± 1.5 S cm$^{-1}$ when $T_s$ was increased from 30 to 300 °C, and then sharply decreased to 647.3 ± 0.4 S cm$^{-1}$ at 340 °C and 414.0 ± 1.2 S cm$^{-1}$ at 380 °C. The enhanced $\sigma$ (=647.3–814.3 S cm$^{-1}$) of the films grown at 220–340 °C originated from the substantially enhanced $\mu$ because the $n$ exhibited a slight decrease (Fig. 4). Although the coupled relationship between $\sigma$ ($=ne\mu$) and $|\alpha|$ ($\sim n^{-2/3}$) generally constrains the concurrent enhancement of $\sigma$ and $|\alpha|$, a reduction of $n$ and a substantial increase of $\mu$ in the same optimal range of $T_s$, 220–340 °C, could lead to high values of both $\sigma$ and $|\alpha|$. Consequently, the PF of the stoichiometric ND, LCP, and LTP films reached remarkably high values, ranging between 18.2 ± 0.25 and 24.3 ± 0.44 μW/cm K$^2$, whereas the PF was low ($\leqslant$0.44 μW/cm K$^2$) in the case of nonstoichiometric films deposited at $T_s \leqslant 120$ or 380 °C (Fig. 5b).

The composition, transport and TE properties at room temperature of the optimal $Bi_2Te_3$ films in this study and those in the earlier relevant studies [13,19–21,23,24,46] are summarized in Table 1. The optimal PF value (24.3 μW cm$^{-1}$ K$^{-2}$) of a layered-compact polycrystalline film obtained in this study was considerably higher than those of the $Bi_2Te_3$ films featuring a nanoparticle structure (PF = 1.9 μW cm$^{-1}$ K$^{-2}$) [20], a layered structure (PF = 8.8 μW cm$^{-1}$ K$^{-2}$) [19], a hexagonal structure (PF = 18.4 μW cm$^{-1}$ K$^{-2}$) [46], and a compact-smooth structure (PF ≈ 21.2 μW cm$^{-1}$ K$^{-2}$) [13]. However, it was slightly lower than the PF = 27 μW cm$^{-1}$ K$^{-2}$ of a smooth epitaxial $Bi_2Te_3$ film grown using MBE [23]. Furthermore, the optimal PF of 24.3 μW cm$^{-1}$ K$^{-2}$ was approximately 1.39-, 1.64-, and 2.08-times lower than the PFs ≈ 33.7, 39.9, and 50.6 μW cm$^{-1}$ K$^{-2}$ of a highly (00l)-oriented layered [21], a hexagonal polycrystalline [24], and a layered smooth films [13], respectively. Generally, as illustrated in Table 1, a stoichiometric composition is necessary to obtain a reasonably low $n$ ($\leqslant 1.0 \times 10^{20}$ cm$^{-3}$) which in turn allows obtaining a high $|\alpha|$ value. Moreover, a layered structure is mostly found to be the best morphology for excellent TE properties (Table 1). In this study, the structure combining both layered and compact features exhibited the highest PF value amongst our films owning to its high $\sigma$ up to 814.3 ± 1.5 S cm$^{-1}$.

The aforementioned results revealed that in this study, $Bi_2Te_3$ thin films prepared using PLD exhibited high PF values at elevated temperatures, at which the PFs of $Bi_2Te_3$ and $Bi_2Se_3$ thin films could be suppressed because of nonstoichiometry and donor-point defects (i.e., vacancies $V_{Te}$ and $V_{Se}$ or antisites $Te_{Bi}$ and $Se_{Bi}$) [15,16]. In this study, a simple deposition strategy was adopted in which the ambient pressure used (80 Pa) was higher than that typically used in PLD depositions (see Table 1), with the goal being to reduce the extent of doping and the $T_s$ (220 °C $\leqslant T_s \leqslant$ 340 °C) for high-$\mu$ preferred structural growth. This approach not only alleviated the doping problem without the requirement of any extra engineering of the targets or engineering during the film growth, but also improved the structural quality of the films and thereby enhanced the charge-carrier mobility and substantially increased PFs. This PLD strategy could potentially be extended to fabricating high-PF thin films on excellent compounds such as $Bi_{2-x}Sb_xTe_3$ and $Bi_2Te_{3-x}Se_x$, promising for applications in TE devices.

## 4. Conclusion

Nanostructured n-type bismuth telluride thin films were fabricated using PLD. At $T_s$ of 220–340 °C and $P_{Ar}$ = 80 Pa, the stoichiometric $Bi_2Te_3$ films with highly (00l)-oriented and layered structures possess remarkably high PFs between 18.2 ± 0.25 and 24.3 ± 0.44 μW cm$^{-1}$ K$^{-2}$, that is attributed to the concurrently substantial enhancements in $\mu$ (83.9–122.3 cm$^2$/Vs) and $|\alpha|$ (172.8–189.7 μV/K). It has been demonstrated that the morphology of highly (00l) oriented-layered structures and the stoichiometry predominantly contribute to the substantial enhancement of $\mu$ and $|\alpha|$, respectively, resulting in remarkable enhancement in PF.

## Acknowledgements

One of the authors (P.H. Le) is thankful for Dr. Hong Quan Nguyen for the help of taking HRTEM images, and Prof. K.H. Wu for the support of using the equipment. Financial support from the Ministry of Science and Technology of the Republic of China (Taiwan) under Contract Nos.: 101-2112-M-009-016-MY2 and 103-2923-M-009-001-MY3 is gratefully acknowledged.

## References

[1] R. Venkatasubramanian, E. Siivola, T. Colpitts, B. O'Quinn, Nature 413 (2001) 597–602.
[2] D.M. Rowe, in: D.M. Rowe (Ed.), Thermoelectrics Handbook: Macro to Nano, CRC/Taylor & Francis, Boca Raton, FL, 2006.
[3] G.J. Snyder, E.S. Toberer, Nat. Mater. 7 (2008) 105.
[4] G.S. Nolas, J. Sharp, H.J. Goldsmid, Thermoelectrics Basic Principles and New Materials Developments, Springer, Berlin, 2001.
[5] H. Böttner, J. Nurnus, A. Gavrikov, G. Kühner, M. Jägle, C. Künzel, D. Eberhard, G. Plescher, A. Schubert, K.-H. Schlereth, J. Microelectromech. Syst. 13 (2004) 414–420.
[6] B. Huang, C. Lawrence, A. Gross, G.-S. Hwang, N. Ghafouri, S.-W. Lee, H. Kim, C.-P. Li, C. Uher, K. Najafi, M. Kaviany, J. Appl. Phys. 104 (2008) 113710.
[7] G. Min, D.M. Rowe, Solid State Electron. 43 (1999) 923–929.
[8] M. Takashiri, T. Shirakawa, K. Miyazaki, H. Tsukamoto, Sens. Actuators A 138 (2007) 329–334.
[9] M. Takashiri, M. Takiishi, S. Tanaka, K. Miyazaki, H. Tsukamoto, J. Appl. Phys. 101 (2007) 074301.
[10] C.-N. Liao, Y.-C. Wang, H.-S. Chu, J. Appl. Phys. 104 (2008) 104312.
[11] M. Takashiri, S. Tanaka, K. Miyazaki, H. Tsukamoto, J. Alloys Comp. 490 (2010) L44–L47.
[12] H.-C. Chang, C.-H. Chen, Y.-K. Kuo, Nanoscale 5 (2013) 7017.

[13] A. Li Bassi, A. Bailini, C.S. Casari, F. Donati, A. Mantegazza, M. Passoni, V. Russo, C.E. Bottani, J. Appl. Phys. 105 (2009) 124307.
[14] R.S. Makala, K. Jagannadham, B.C. Sales, J. Appl. Phys. 94 (2003) 3907.
[15] L.M. Goncalves, C. Couto, P. Alpuim, A.G. Rolo, F. Völklein, J.H. Correia, Thin Solid Films 518 (2010) 2816–2821.
[16] P.H. Le, C.-N. Liao, C.W. Luo, J.-Y. Lin, J. Leu, Appl. Surf. Sci. 285P (2013) 657–663.
[17] N. Peranio, M. Winkler, D. Bessas, Z. Aabdin, J. König, H. Böttner, R.P. Hermann, O. Eibl, J. Alloys Comp. 521 (2012) 163–173.
[18] A. Mzerd, D. Sayah, J.C. Tedenac, A. Boyer, J. Cryst. Growth 140 (1994) 365.
[19] Y. Deng, H.-M. Liang, Y. Wang, Z.-W. Zhang, M. Tan, J.-L. Cui, J. Alloys Comp. 509 (2011) 5683–5687.
[20] H.-C. Chang, C.-H. Chen, CrystEngComm 13 (2011) 5956–5962.
[21] Z. Zhang, Y. Wang, Y. Deng, Y. Xu, Solid State Commun. 151 (2011) 1520–1523.
[22] Y. Zhou, L. Li, Q. Tan, J.-F. Li, J. Alloys Comp. 590 (2014) 362–367.
[23] N. Peranio, O. Eibl, J. Nurnus, J. Appl. Phys. 100 (2006) 114306.
[24] H. Zou, D.M. Rowe, G. Min, J. Cryst. Growth 222 (2001) 82–87.
[25] A. Bailini, F. Donati, M. Zamboni, V. Russo, M. Passoni, C.S. Casari, A. Li Bassi, C.E. Bottani, Appl. Surf. Sci. 254 (2007) 1249–1254.
[26] L.S. Faraji, R.P. Singh, M. Allahkarami, Eur. Phys. J. Appl. Phys. 46 (2009) 20501.
[27] L.R. Testardi, G.K. McConnell, Rev. Sci. Instrum. 32 (1961) 1067.
[28] J.A. Thornton, J. Vac. Sci. Technol. 11 (1974) 666.
[29] J.A. Thornton, J. Vac. Sci. Technol. 12 (1975) 830.
[30] T. Karabacak, J.P. Singh, Y.-P. Zhao, G.-C. Wang, T.-M. Lu, Phys. Rev. B 68 (2003) 125408.
[31] M. Ohring, The Materials Science of Thin Films, Academic Press, San Diego, CA, 1992.
[32] D.L. Smith, Thin-Film Deposition: Principles & Practice, McGraw-Hill, New York, 1995.
[33] D. Kong, W. Dang, J.J. Cha, H. Li, S. Meister, H. Peng, Z. Liu, Y. Cui, Nano Lett. 10 (2010) 2245–2250.
[34] Y. Liang, W. Wang, B. Zeng, G. Zhang, J. Huang, J. Li, T. Li, Y. Song, X. Zhang, J. Alloys Comp. 509 (2011) 5147–5151.
[35] G. Hao, X. Qi, L. Yang, Y. Liu, J. Li, L. Ren, F. Sun, J. Zhong, AIP Adv. 2 (2012) 012114.
[36] Y. Deng, Y. Xiang, Y. Song, Cryst. Growth Des. 9 (2009) 3079–3082.
[37] C.-N. Liao, H.-D. Shih, P.-W. Su, J. Electrochem. Soc. 157 (2010) D605–D608.
[38] S.X. Zhang, L. Yan, J. Qi, M. Zhuo, Y.-Q. Wang, R.P. Prasankumar, Q.X. Jia, S.T. Picraux, Thin Solid Films 520 (2012) 6459–6462.
[39] H. Noro, K. Sato, H. Kagechika, J. Appl. Phys. 73 (1993) 1252.
[40] P.H. Le, K.H. Wu, C.W. Luo, J. Leu, Thin Solid Films 534 (2013) 659–665.
[41] S. Cho, Y. Kim, A. DiVenere, G.K. Wong, J.B. Ketterson, J.R. Meyer, Appl. Phys. Lett. 75 (1999) 1401.
[42] A. Hashibon, C. Elsässer, Phys. Rev. B 84 (2011) 144117.
[43] G. Wang, X.G. Zhu, Y.Y. Sun, Y.Y. Li, T. Zhang, J. Wen, X. Chen, K. He, L.L. Wang, X.C. Ma, J.F. Jia, S.B. Zhang, Q.K. Xue, Adv. Mater. 23 (2011) 2929.
[44] J.W.G. Bos, H.W. Zandbergen, M.-H. Lee, N.P. Ong, R.J. Cava, Phys. Rev. B 75 (2007) 195203.
[45] H.S. Shin, S.G. Jeon, J. Yu, Y.-S. Kim, H.M. Park, J.Y. Song, Nanoscale 6 (2014) 6158–6165.
[46] L.W. da Silva, M. Kaviany, C. Uher, J. Appl. Phys. 97 (2005) 114903.